Immersed Boundary Wall-Modelled Large Eddy Simulations of a Generic Hammerhead Payload Fairing

Gaetan K. W. Kenway *, Aditya S. Ghate, Oliver M. F. Browne, Man Long Wong, Jordan B. Angel, and Cetin C. Kiris
Volcano Platforms Incorporated, Palo Alto, CA 94304, USA

Wall-Modelled Large Eddy Simulations (WMLES) are performed to study the vibro-acoustics environment on a generic "hammerhead" shaped payload fairing studied experimentally by Coe & Nute in 1962, and more recently by Schuster et al. (2016) at NASA Ames Research Center. The Mach 0.8, $\alpha = 4°$ case is selected for its particularly challenging character: supersonic flow sets in at two locations on the fairing with incipient shock-induced boundary layer separation causing large pressure fluctuation spikes on the payload fairing. Comparisons of pressure spectra on the frustum of the payload fairing (location of peak pressure root-mean-square) and the second stage show good agreement with Kulite data across 4 decades of frequency range. Furthermore, two-point space-time correlations of pressure fluctuations on this portion of the geometry indicate a convection velocity of approximately $0.6 \times U_\infty$ which is consistent with the findings of Panda et al. (2018). Major discrepancies between experimental data and simulation are observed in *quieter* parts of the flow such as nose of the fairing, and the locally supersonic regions between the two normal shocks on the payload fairings. LES predicts pressure fluctuations with orders of magnitude smaller in intensity than the Kulite measurements in these locations. Additional investigation into tunnel background noise, as well as LES grid resolution in the boundary layers is needed to understand these discrepancies.

I. Introduction

The design of space launch vehicles is exceptionally complex. One challenging aspect, is the accurate prediction of the aerodynamic loads as the vehicle ascends through the lower atmosphere. As the rocket accelerates toward orbital velocity, it passes through the transonic flight regime (Mach number, M = 0.8-1.1). During this period of flight, the unsteady aerodynamic loading can be quite severe, potentially causing damage to the launch vehicle or its payload. Payload fairings are light-weight large-diameter coverings that shield the spacecraft's payload while it transits the dense, lower atmosphere. Often, the fairing diameter is larger than that of the remainder of the rocket. This type of payload fairing has been known as a "hammerhead" configuration. Many contemporary examples of hammerhead shaped payload fairings are the variants of the Falcon 9, Vega, Long March, and Atlas rockets, among others.

Buffet is the cyclic loading of a vehicle caused by unsteady aerodynamic loading. While buffet can occur at any Mach number, *transonic buffeting* can be particularly problematic for rockets since it usually occurs when the vehicle is at, or close to its maximum dynamic pressure. In this regime there are complex interactions between shock waves and boundary layer separation which can cause very high unsteady loads to be imparted on the vehicle. These loads can in turn cause structural problems, such as vehicle bending loads, structural panel oscillations and damage to equipment or electronics due to vibrations [1, 2]. Hammerhead configurations turn out to be particularly sensitive to the effects of transonic buffeting and this problem has been known since the beginning of the space-age over 60 years ago. The geometry that will be studied in this work was initially described by Coe and Nute [3]. In that work, three different hammerhead-like configurations were tested in the NASA Ames Research Center (ARC) 11 foot transonic wind tunnel at Mach numbers varying between M = 0.6-1.1. The experiments were part of a NASA effort to experimentally characterize transonic buffeting and to generate empirical guidelines that would guide the design of future rockets [1]. Even after nearly a half century of wind-tunnel and flight test experience, transonic buffet remains an issue on modern rockets. A NASA "Lessons Learned" note from 2015 reiterated the need to adhere to long-standing design principles of payload fairings to reduce the effects of buffet. Two recent payload fairing designs used Reynolds-Averaged Navier–Stokes (RANS) code during the initial design phase. When the final designs were tested in a wind tunnel, buffet issues were discovered and required costly redesigns. To directly quote the Lessons Learned [4]:

"A second lesson is to avoid using codes which cannot check whether such [buffeting] behavior can occur. The second lesson follows from the current practice of using Reynolds-Averaged Computational Fluid

*Corresponding author.

Dynamics CFD codes to predict the vehicle flow behavior and acquire loads for the initial databases. Such codes are not capable of predicting the kinds of flow behavior that violating the NASA Guidelines can produce. Hence, a false sense of security can prevail unless the Guidelines are known and promulgated to the designers and analysts."

The main goal of this work is to critically evaluate the use of Computational Fluid Dynamics (CFD) using methods that are "beyond RANS". In particular, Wall-Modelled Large Eddy Simulation (WMLES) methods have been increasingly replacing legacy CFD techniques such as RANS in problems involving large scale flow separation [5–7], as well as for aeroacoustics [8, 9]. However, the use of WMLES in problems involving shock-induced separation is largely limited to canonical problems [10–13]. This is unfortunate, since majority of industrial problems involving shock-boundary layer interactions often require prediction of unsteady pressure loading - WMLES is particularly suited for such applications due to large length scales associated with instantaneous wall-pressure fluctuations (as opposed of instantaneous skin-friction) [14]. Use of scale-resolving simulations for predicting vibroacoustic environment of launch vehicles is in its nascency. All prior work [15–18] has involved use of hybrid RANS/LES techniques which tend to model only the separated regions of the flow using an LES closure. Present work takes a starkly different approach - we attempt to model all scales of of motion including the attached boundary layer and its onset via obstructive tripping using a purely LES closure along with equilibrium modeling of the viscous inner layer (wall-modeling). A new immersed boundary WMLES code, Volcano ScaLES, utilizing octree Cartesian grids is used. We hope to show that modern, state-of-the-art CFD methods are capable of accurately predicting the vibroacoustic environment on launch vehicles, and thus can be used to evaluate designs that violate the decades old guidelines. For this work, we choose to focus on Coe and Nute's "Model 11" configuration [3] which has the largest diameter payload fairing. Furthermore, a recent test campaign was undertaken at NASA ARC to re-test the "Model 11" configuration [19, 20]. The main goal of the modern test campaign was to generate high quality experimental data for use in validating modern CFD methods for predicting vibroacoustics in this critical flight regime, and Kulite (unsteady pressure) data from this campaign will be utilized to assess the accuracy of the LES predictions. A schematic of the Model 11 configuration along with the placement of key Kulites used for comparisons is shown in Figure 1.

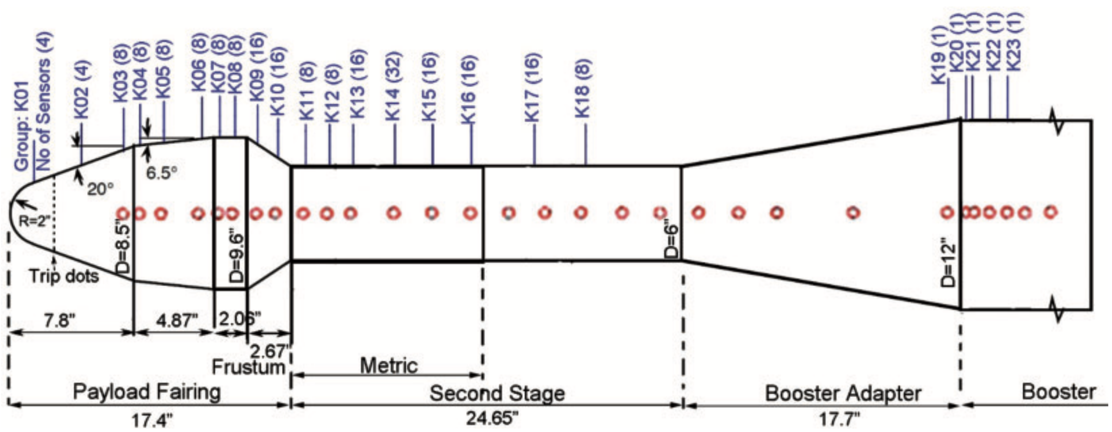

Fig. 1 Schematic of hammerhead payload fairing configuration (Model 11). Reproduced from [20].

The remainder of this paper is outlined as follows: a brief description of the simulation details is given in Section 2. In Section 3, this algorithm is first validated for transonic shock-boundary layer interactions using the classic ONERA M6 wing at Mach 0.84. In Section 4, WMLES time-averaged and instantaneous surface pressure loads for the hammerhead payload fairing are compared with experimental data. Finally, in Section 5 a brief summary of observations along with potential future research directions is presented.

II. Simulation Details

A. Numerical Formulation

Volcano ScaLES solves the compressible Navier–Stokes equations using a nominally fourth order spatially accurate finite difference discretization with favorable Kinetic Energy and Entropy Consistency properties making it suitable for large eddy simulations (LES) over a vast range of flow regimes. The viscous flux discretization utilizes a mix of fourth order and second order discretizations with high spectral bandwidth thereby allowing further robustness for high Reynolds number flows without additional numerical dissipation via the inviscid flux numerical operator in turbulence resolving regions. Physics-based numerical sensors that are functions of local velocity gradients as well as pressure and density fluctuations allow for spatio-temporally localized use of limiters needed to capture flows with discontinuities such as shocks and steep density gradients. A key convenience afforded by the use of Cartesian grids with unit aspect ratio is the use of explicit time-stepping scheme even in flows involving highly complex geometries; the perfectly isotropic grid cells near the geometry do not introduce any numerical stiffness associated with complex grid topologies. The popular Strong Stability Preserving (SSP) variant of the classical third order Runge–Kutta scheme developed by Gottlieb and Shu [21] is utilized for all the work presented in this paper.

Geometries are represented in the numerical formulation using an immersed boundary algorithm capable of enforcing inviscid no-penetration boundary conditions as well as viscous skin friction with appropriate Reynolds number asymptotic properties using an equilibrium wall-model. The wall-model that provides a shear-stress constraint at the wall uses solution information interpolated via probing at a fixed distance of $3\Delta/2$ into the fluid away from walls, where Δ is the local grid spacing. Additional numerical techniques to damp generation of spurious numerical noise at walls as well as at coarse-fine interfaces are also utilized. All simulations presented in this work utilize the dynamic Smagorinsky model [22, 23] to model the subgrid-scale stresses.

The CFD solver has been validated using a sequence of WMLES including: a) subsonic jets [24], b) airframe noise [25], c) aerodynamics of iced straight wings [26], d) F-16XL aircraft aerodynamics [27], and e) automotive aerodynamics [28].

B. Cartesian Octree Grid System

Volcano ScaLES employs Cartesian grids generated using a recursive octree-refinement approach. The advantages of Cartesian meshes include significantly reduced memory requirements and simple, high-accuracy numerical formulations. For most practical problems, many mesh resolutions are required, which introduces coarse-fine interfaces between mesh levels. In ScaLES, cubic interpolation schemes are used to transfer data from one grid level to another. Grids for practical configurations, such as the one presented in this paper, consist of an unstructured layout of millions of "boxes", each of which contains a structured grid of either 8^3 or 4^3 cells. This method yields nearly all the computational advantages of a globally structured grid, while retaining the ability to closely follow surfaces and minimize the number of "dead" cells inside the geometry. Typically, 90-95% of the total cells in a grid are "live" compute cells, where the partial differential equations are solved.

C. Computational Architecture

Motivated by the need to fully exploit all available resources on modern GPUs, Volcano ScaLES is written in C++ and CUDA. On simulations involving non-canonical geometries, such as those considered in this paper, we achieve approximately 30% of peak FLOPs on compute-oriented devices along with nearly perfect (>95%) weak scaling efficiency from 1 to 8 GPUs. Unlike most CFD codes, the majority of the computations are compute bound and we achieve high performance even in graphics-oriented, bandwidth-restricted devices, such as the Nvidia RTX 4090. The combination of Cartesian methods and an explicit time stepping scheme yields extremely low memory requirements: ScaLES can simulate between 8.5 and 10 millions cells per gigabyte of GPU memory depending on the complexity of the configuration.

III. Validation Test Case for Shock-Boundary Layer Interactions: The ONERA M6 Wing

The ONERA M6 wing case at $M = 0.84$ and $Re = 14.6 \times 10^6$ (based on the root chord) is simulated at an angle-of-attack of $\alpha = 3.06°$ [29, 30]. This transonic flow case represents a challenging problem for WMLES given the complex flow physics, namely: shock-wave/boundary-layer interactions particularly at outboard section of the wing, multiple shocks including a lambda shock, strong sensitivity in the shock location based on the transition location at the leading edge of the wing, *etc*. A coarse and fine grid system are utilized in the simulations with the details given in Table 1 and Figure 2 shows the distribution of the grid point levels in the volume and on the wing surface for the fine grid.

Figure 3 shows an instantaneous visualization of the pressure coefficient and x-component of skin friction coefficient on the surface of the wing obtained with the fine grid. The lambda shock structure can be seen on of the wing with a small region of shock induced boundary-layer separation visible behind the shock at the outboard region of the

Table 1 Details of the WMLES for the ONERA M6 wing problem.

Name	Total compute cells (M)	Compute cells on finest level (M)	Min. grid spacing (mm)	Approx. time-step size (μs)
Coarse	305	130	0.2	0.195
Fine	1230	626	0.119	0.117

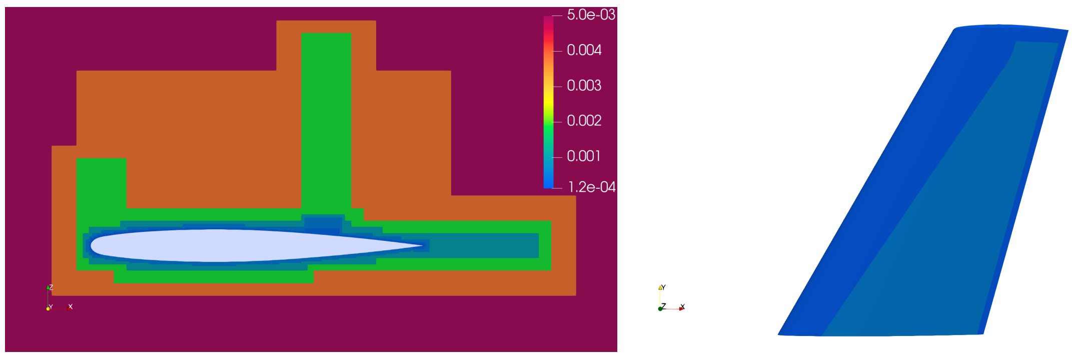

(a) xz-plane

(b) Grid spacing near the surface

Fig. 2 Grid size distribution for the ONERA M6 wing at η = 0 and on the surface.

wing. The boundary-layer appears to transition relatively quickly at the leading edge of the wing (< 5% of the chord) and moves upstream with grid refinement (not shown). Figure 4 shows time-averaged surface pressure coefficient curves obtained on the coarse and fine grids and compared to experimental wind tunnel data [29] and a RANS solution (FUN3D RANS-SA-neg results obtained from NASA Langley Turbulence Modeling Resource website [30]. Overall, good agreement in the prediction surface pressure, including the location of the shocks, is seen for both coarse and fine grid resolutions with experimental data and RANS. At $\eta = 0.9$ WMLES shows a slight overshoot in the pressure recovery when compared to experiment and RANS. Finally, at $\eta = 0.99$ WMLES shows a slightly improved prediction of the surface pressure, when compared to RANS, downstream of the shock between $x/c = 0.8$ and $x/c = 1.0$.

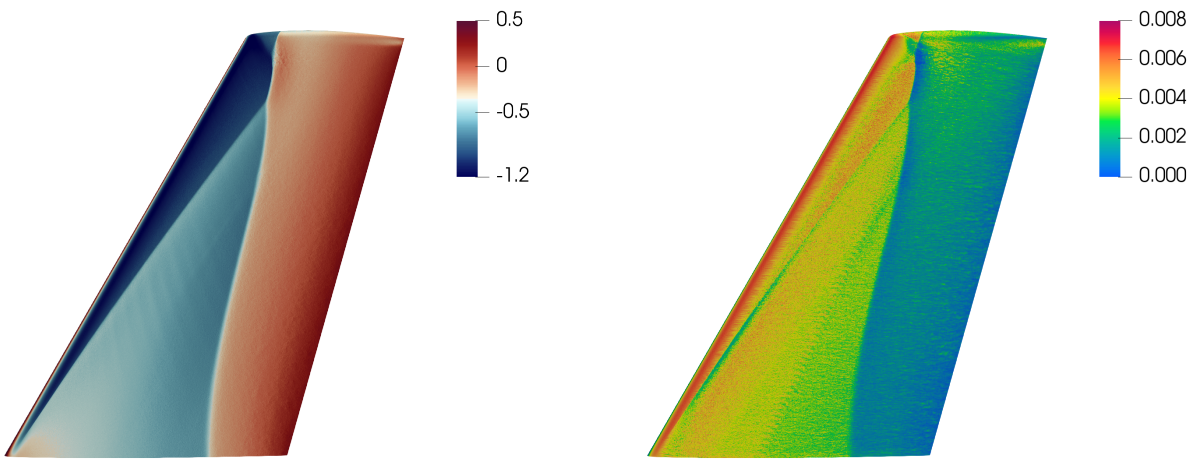

(a) pressure coefficient

(b) x-component of skin friction coefficient

Fig. 3 Instantaneous surface (a) pressure coefficient and (b) x-component of skin friction coefficient on the fine grid for the ONERA M6 wing at α = 3.06 and M = 0.84.

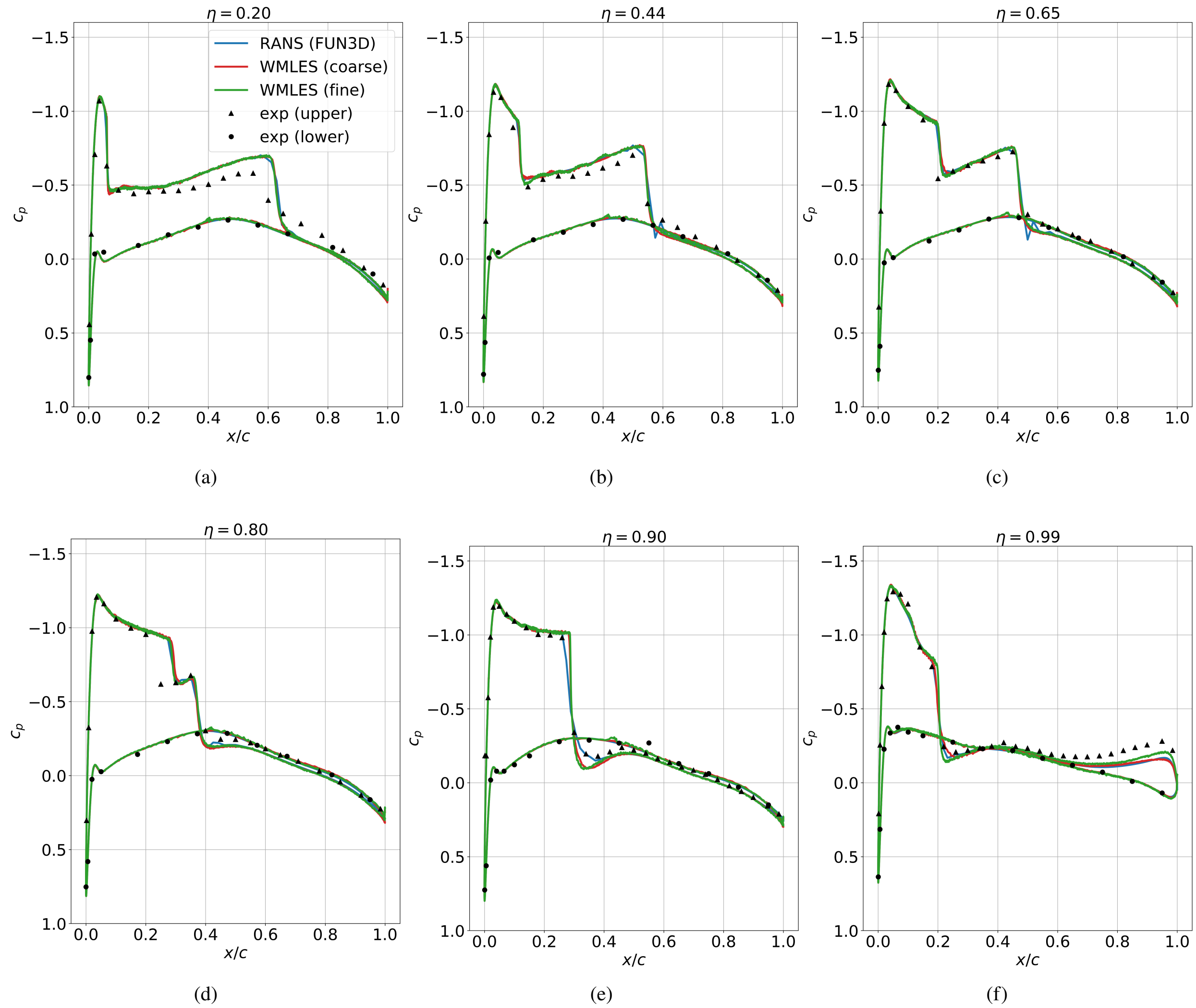

Fig. 4 Time-averaged surface pressure coefficients curves along the span of the ONERA M6 wing at α = 3.06 and M = 0.84.

IV. Hammerhead Payload Fairing

A. Case Details

The $\alpha = 4°$, Mach 0.8 case at a Reynolds number of 3×10^6/ft is studied. Obstructive tripping is employed near the nose of the fairing to trigger a turbulent boundary layer, consistent with the Ames experiment. The basic flow characteristics observed are shown in Figure 5. The strongly favorable pressure gradient on the nose of the fairing leading up to the front shock results in a very thin boundary layer. This portion of the geometry poses the strictest resolution requirements for the problem. The boundary layer thickens downstream of the shock, but the subsequent favorable pressure gradient seen on the tapered portion of the fairing leads to further quenching of boundary layer turbulence due to acceleration leading up to the second normal shock. The instantaneous surface pressure fluctuations are seen downstream of the leading lambda shock due to incipient separation resulting from the strong normal shock as shown in Figure 5. The pressure fluctuations have an integral length scale representative of boundary layer thickness and have very short decorrelation time-scales. The two shocks on the payload fairing require additional resolution beyond the near-wall resolution requirements of the vorticity dominant flow. The taper at the aft end of the payload fairing leads to separated flow on the leading portion of the second stage which experiences the largest amplitude pressure oscillations.

Unlike the pressure fluctuations downstream of the front lambda shock, the pressure fluctuations downstream of the payload fairing are due to very large scale structures influenced by the geometric length scale of the model (taper angle, etc.). These large-time scale motions represent by far the largest vibro-acoustic loading on the geometry. Fine-grid resolution requirement in this portion of the geometry is dominated by the shear-layers associated with the separated flow.

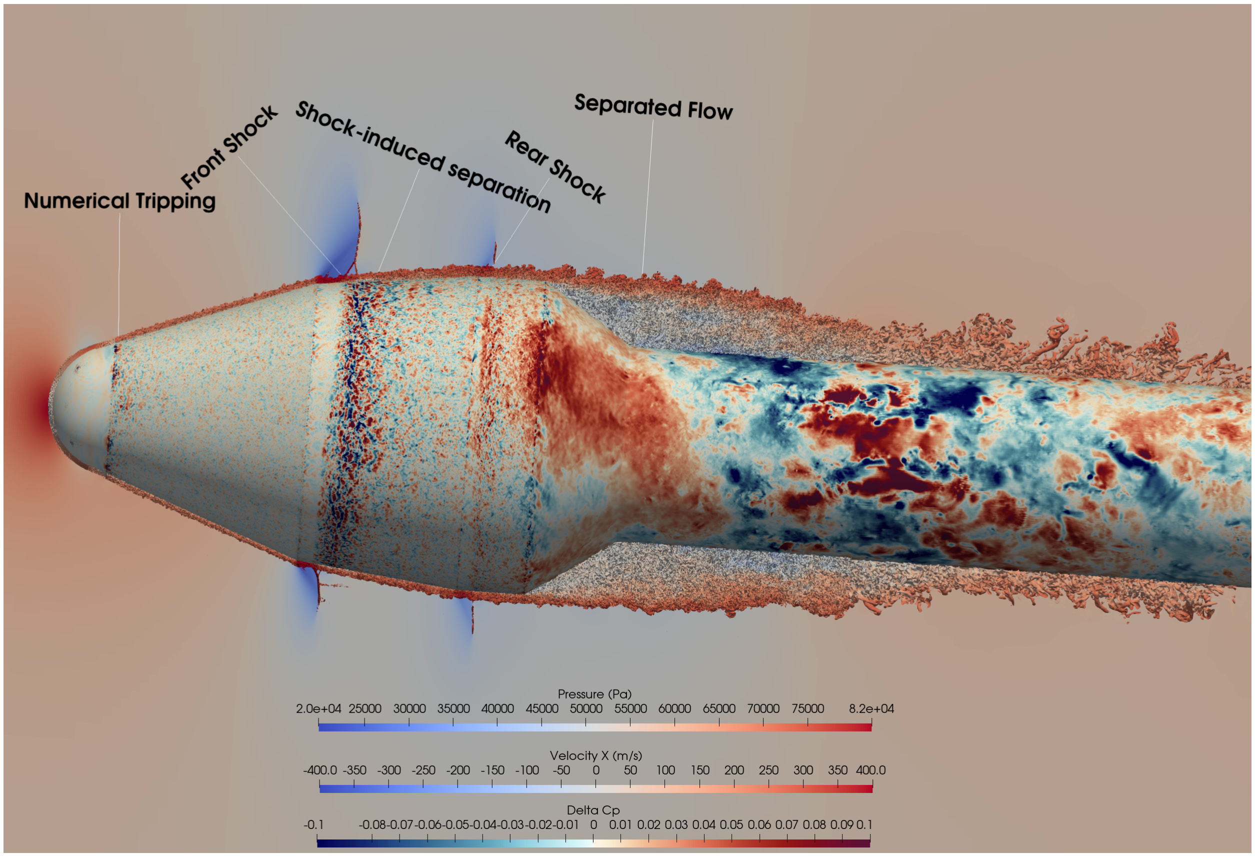

Fig. 5 Overview of the important features of the solution. Q-criterion iso-surfaces are colored by x-velocity. The surface shows the difference between mean C_p and instantaneous C_p at one snapshot in time. The background is the instantaneous pressure field computed using grid A.

B. Grid-Topology Employed

Based on the flow physics discussed above, the grid topology shown in Figure 6 is employed. The finest grid level is used to capture the thin turbulent boundary layer on the nose and the tapered section of the payload fairing leading up to the shear layer forming on the neck/frustrum of the fairing. Additional volume refinement at the second finest level is employed to resolve two shocks on the payload fairing. As the boundary layer further downstream on the metric portion of the second stage is thick, coarser grid levels are employed to reduce the overall grid count. With this base grid topology fixed, two grids are generated. Table 2 provides details of the two grid systems.

Table 2 Details of the WMLES for the hammerhead problem.

Name	Total compute cells (M)	Compute cells on finest level (M)	Min. grid spacing (mm)	Approx. time-step size (μs)
Grid A	454	142	0.220	0.25
Grid B	652	194	0.1875	0.21

G

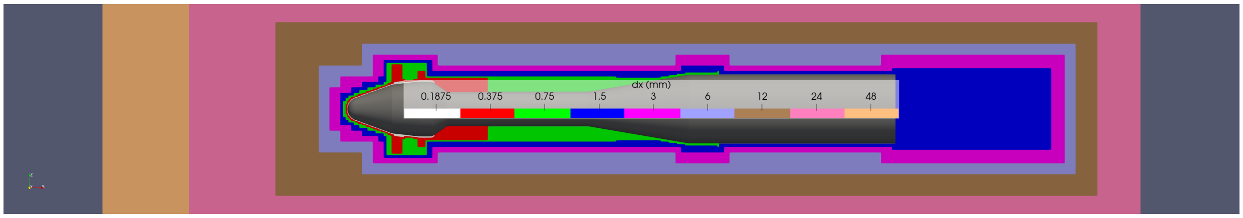

(a) Overview

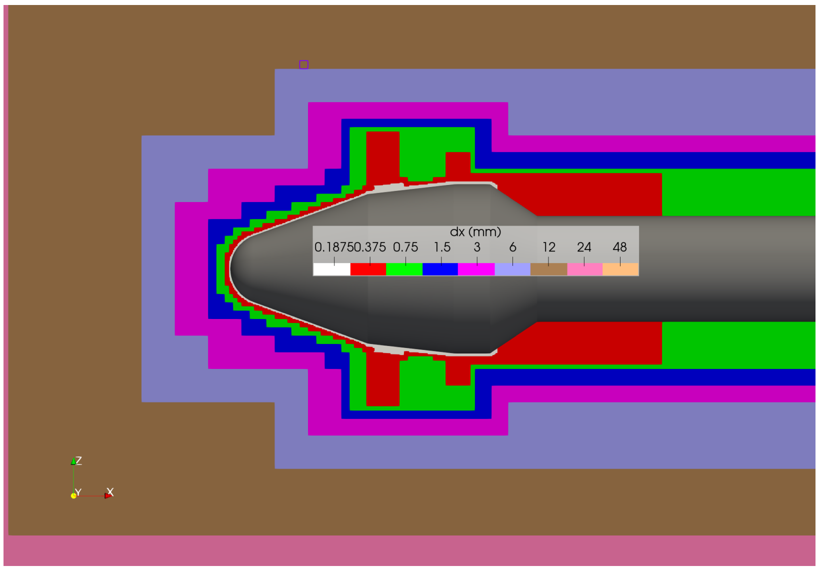

(b) Close-up view on the payload fairing

Fig. 6 Grid topology for the two meshes considered using grid B as an example.

C. Time-Averaged Surface Pressure

Figure 7 shows the azimuthal time-averaged pressure distribution along the geometry compared with the experimental data from Coe & Nute as well as the more recent experiment of Schuster et al. Figure 8 shows root-mean-square (RMS) of the pressure fluctuations on both the surface as well as on the centerline-plane ($y = 0$). Several observations can be made using these two time-averaged fields:

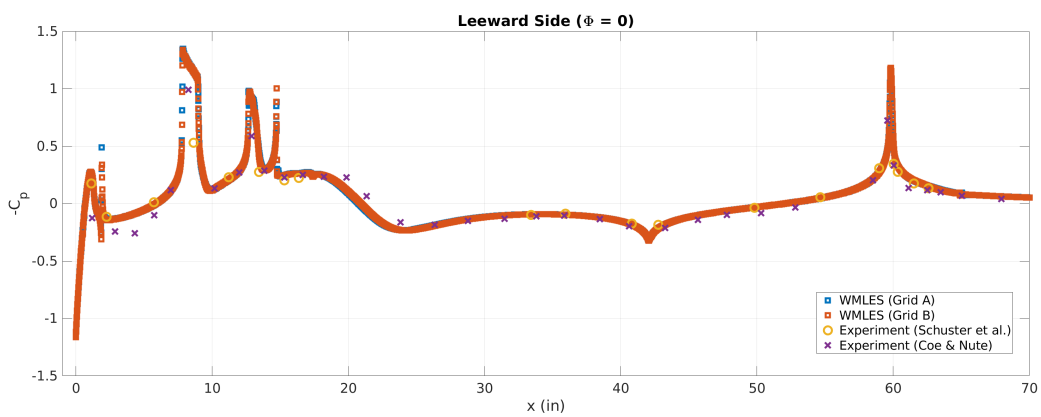

Fig. 7 Time averaged surface pressure coefficient (C_p) along the azimuth ($\phi = 0°$).

1) LES appears to predict the two shock-locations with reasonable accuracy. Due to limited and granular nature of

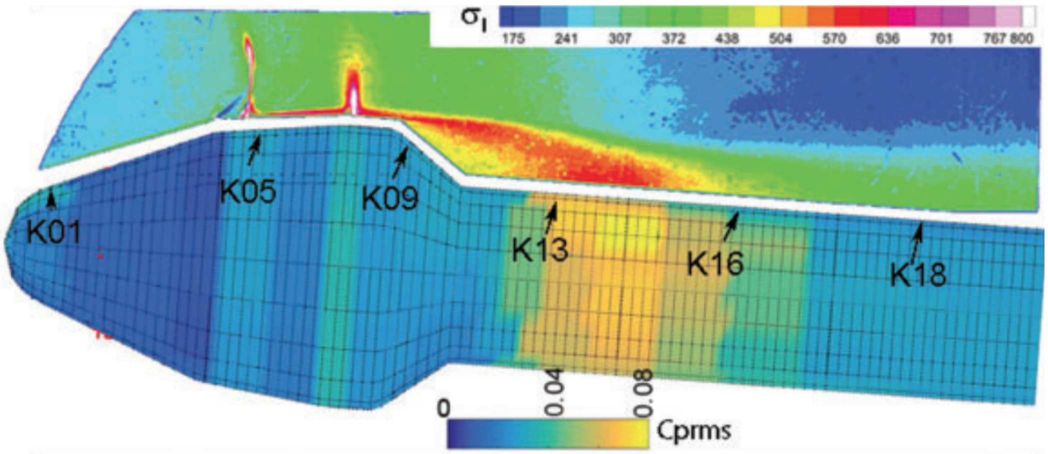

(a) NASA Ames Experiment

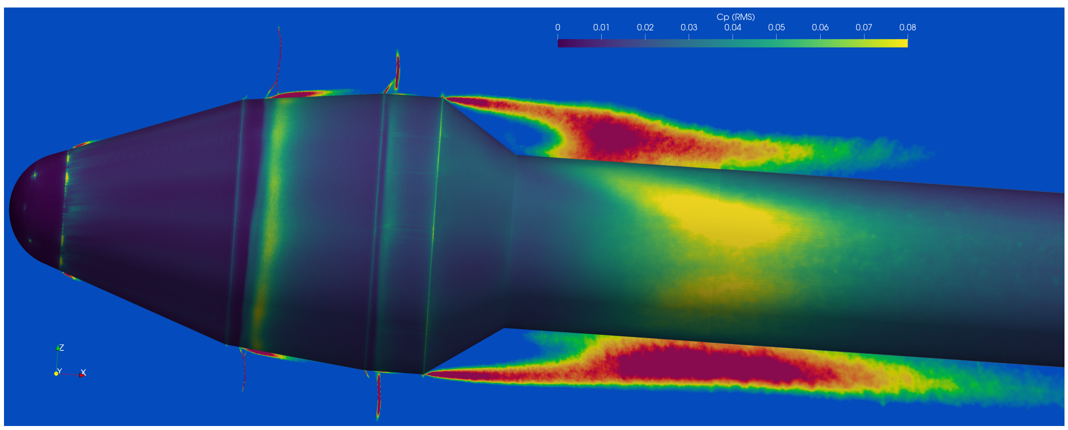

(b) Grid B simulation

Fig. 8 Experimental data (a) from [20] showing the C_p RMS on the surface. The same quantity is shown for the (b) fine grid simulation and (c) the coarse grid simulation.

the measurements available high-resolution detailed comparisons are not possible; however, it appears that two peaks associated with the normal shocks are in good agreement. Interestingly on the nose section of the fairing ($x < 10\ in$), LES appears to agree with the more recent Schuster et al. experimental campaign compared to the Coe & Nute's data.

2) When compared against Coe & Nute's data, the experiment shows a larger separation bubble downstream of the fairing but at this stage the cause of this difference is unclear. One potential cause could be the difference in Reynolds number; the LES was performed at the Reynolds number seen in the Schuster et al.'s experiment while Coe & Nute's experiment had a Reynolds number approximately 33% higher. Inverse Reynolds number scaling of separation bubble sizes have been observed on smooth body separation problems[31, 32].
3) Little sensitivity is observed between the two grid levels in prediction of time-averaged pressure coefficient.
4) The unsteadiness associated with the front lambda-shock structure shows good qualitiative agreement when the RMS of C_p is compared against the fluctuation intensity characterization from the experiment. Similarly the rear shock shows larger deviation compared to the front shock which appears to be consistent with the experiment.
5) The peak surface pressure unsteady loading occurs on the second stage downstream of the the payload fairing at an azimuthal angle, $\phi \approx 50°$ instead of the azimuth ($\phi = 0°$). The surface pressure variance reconstructed using the experimental Kulite data appears to show a consistent trend where the peak pressure RMS occurs somewhere between K13 and K16 at a non-zero azimuthal angle within the first quadrant ($0° < \phi < 90°$).

D. Unsteady Surface Pressure

The unsteady pressure is characterized using two metrics - a) auto-spectra (power spectral density) of pressure compared with Kulite data, and b) Two-point space-time correlations between Kulite pairs to approximate convective velocity. The comparisons between experiment and WMLES are shown in several figures from Figure 9 through Figure 15. Several important observations follow:

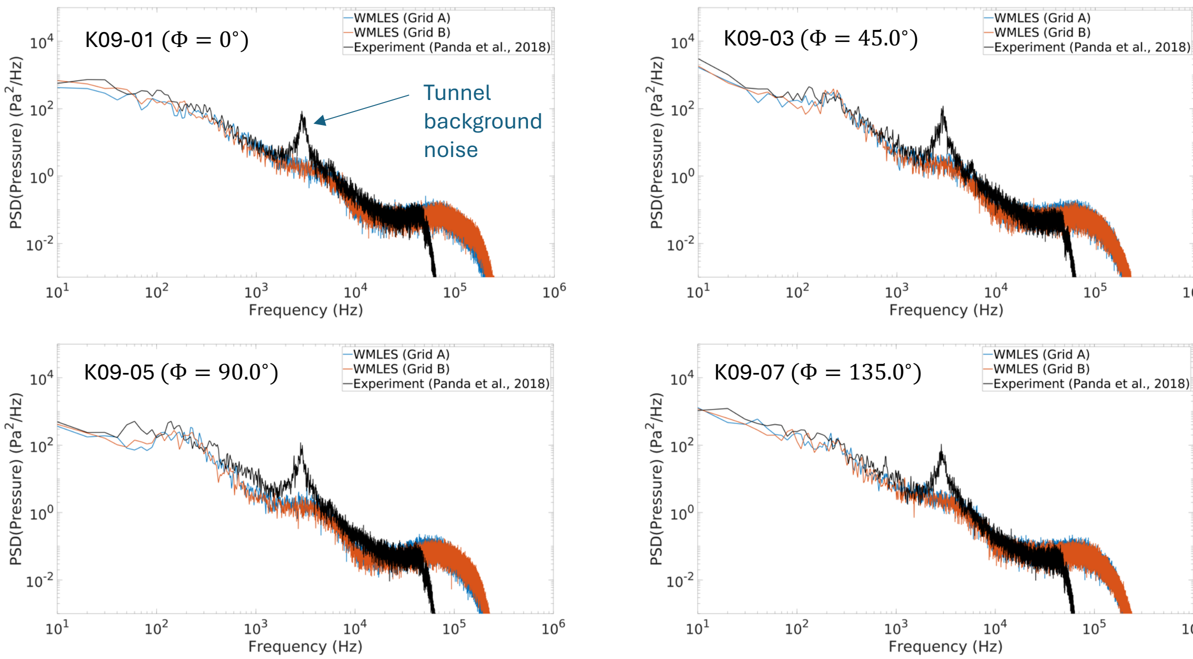

Fig. 9 Pressure auto-spectra on the Kulite 9 row located on the neck/frustrum of the payload fairing.

1) Auto-spectra on various locations along the neck of the fairing as well as the second stage show promising agreement between the experiment and the WMLES over a very wide range of frequencies (10 Hz through 60,000 Hz) (Figures 9 - 11. Certain *quiet* Kulite locations such as the K09 and K10 rows contain tunnel background contamination seen as a tone at approximately 2000 Hz which is noticeably absent in the free-air WMLES. Apart from this, the agreement is good at a variety of circumferential angles especially on the upstream regions of the second stage and the fairing neck.
2) Further downstream at K-4 WMLES underpredicts the energy in the low-frequencies noticeably (Figure 12). At this time the cause of this under-prediction is unclear, especially since both grids A and B produce essentially identical autospectra. However, with increasing circumferential angles the agreement is excellent. Grid topology employed for the current simulations contain entirely axisymmetric grid systems; this may need to be revisited in the future for the 4° angle of attack case being studied. Underprediction of low-frequencies along the $y = 0$ plane ($\phi = 0°$ and $\phi = 180°$) with increasing downstream distance on the second stage is particularly perplexing since it corresponds to very large scale motions. Errors in such large-scale fluctuations could be a result of small differences in the size of the separated flow region thereby changing the shear-layer formed downstream of the fairing.
3) While the pressure spectra on the second stage and the fairing neck is quite promising this is most certainly not the case for pressure fluctuations on the nose and the flat regions of the fairing (Figure 13). While these *quite* regions of the flow are likely to suffer from a larger influence of tunnel background noise, the grid sensitivity observed on K07-01 suggests that substantially finer grids may be needed on to resolve the thin boundary layers on the fairing in order to get any potential shock-boundary layer unsteadiness accurately. Closer inspection of the solution also indicates the possibility of flow laminarization between K04 and K05 due to strong acceleration downstream of the front lambda shock. Additional grid resolution would be needed to confirm accuracy of this behavior. Panda et al (2019) [33] have identified similar differences between Kulite and unsteady Pressure

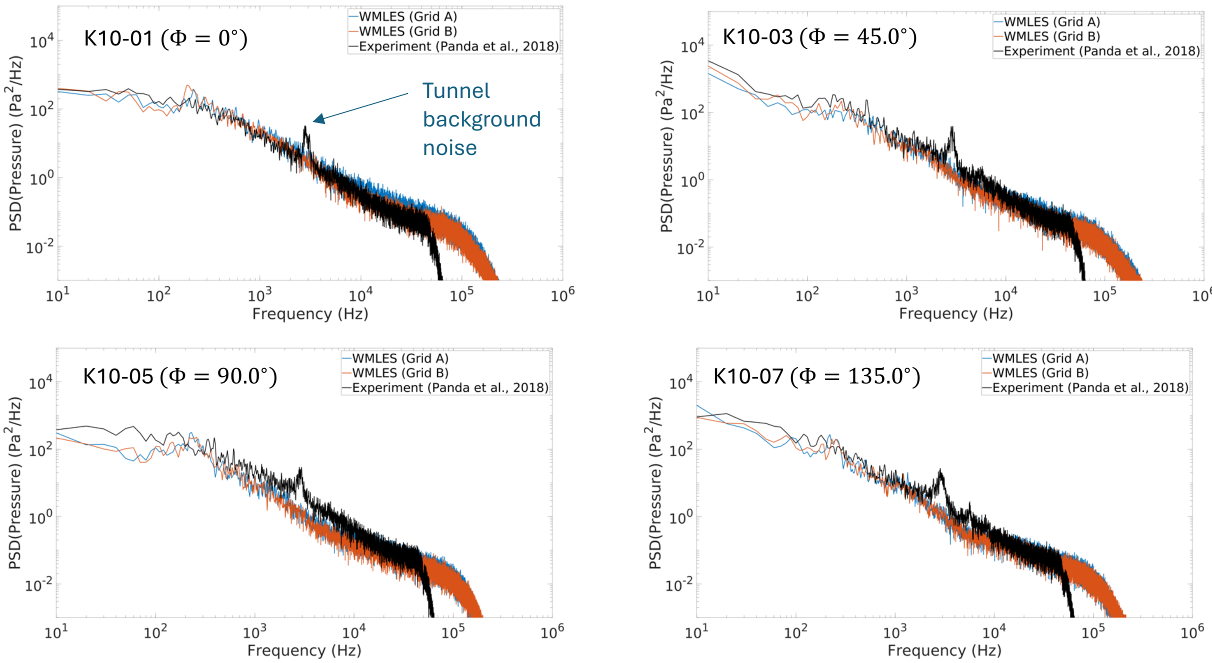

Fig. 10 Pressure auto-spectra on the Kulite 10 row located on the neck/frustrum of the payload fairing.

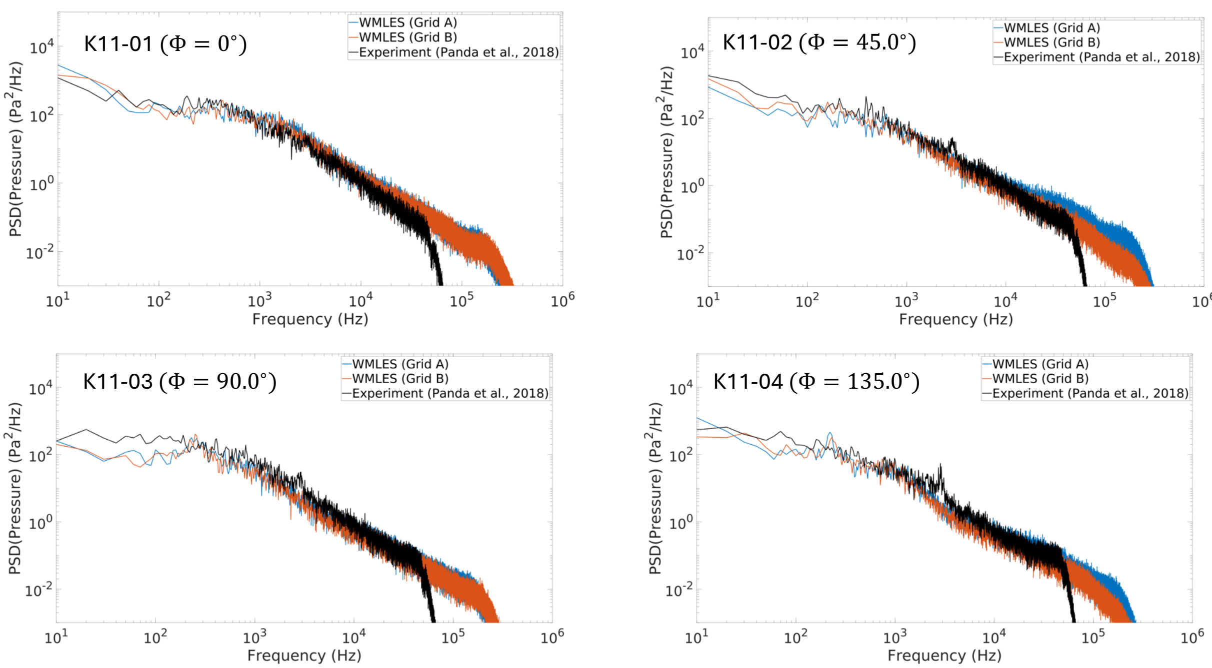

Fig. 11 Pressure auto-spectra on the Kulite 11 row located on the metric portion of the second stage.

Sensitive Paint (uPSP) in these regions of the flow further adding to the uncertainties regarding this comparison between experiment and WMLES.

4) Figure 14 shows the temporal correlation between pairs of Kulite located on the second stage around the vicinity

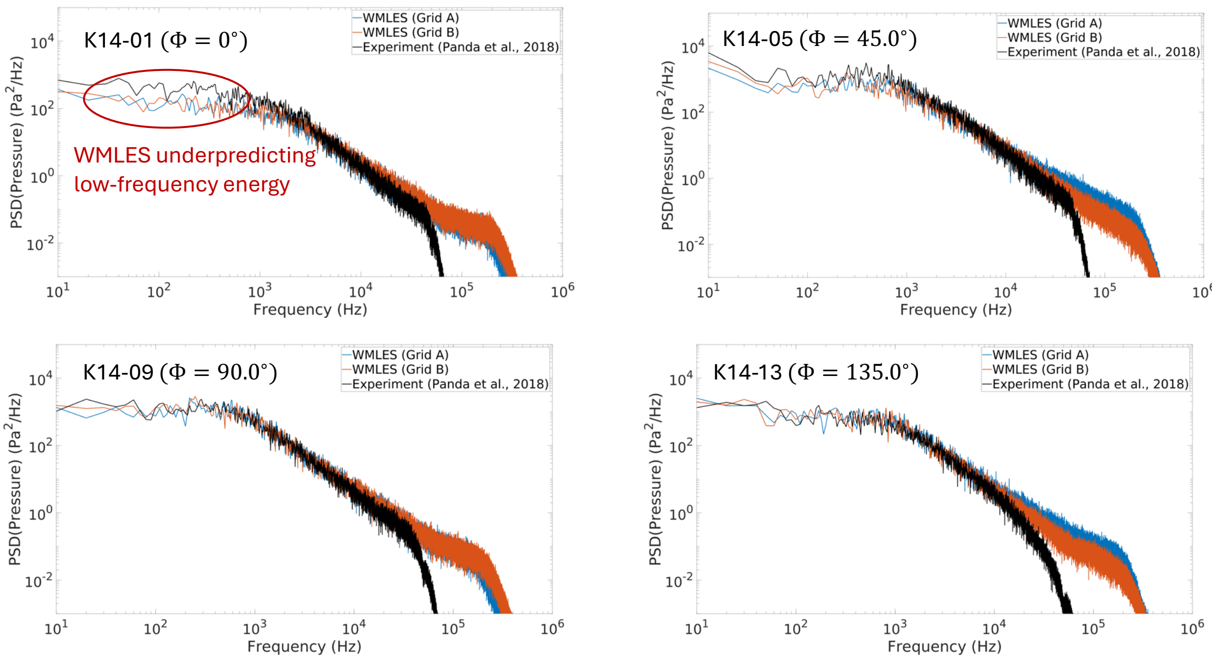

Fig. 12 Pressure auto-spectra on the Kulite 14 row located on the metric portion of the second stage.

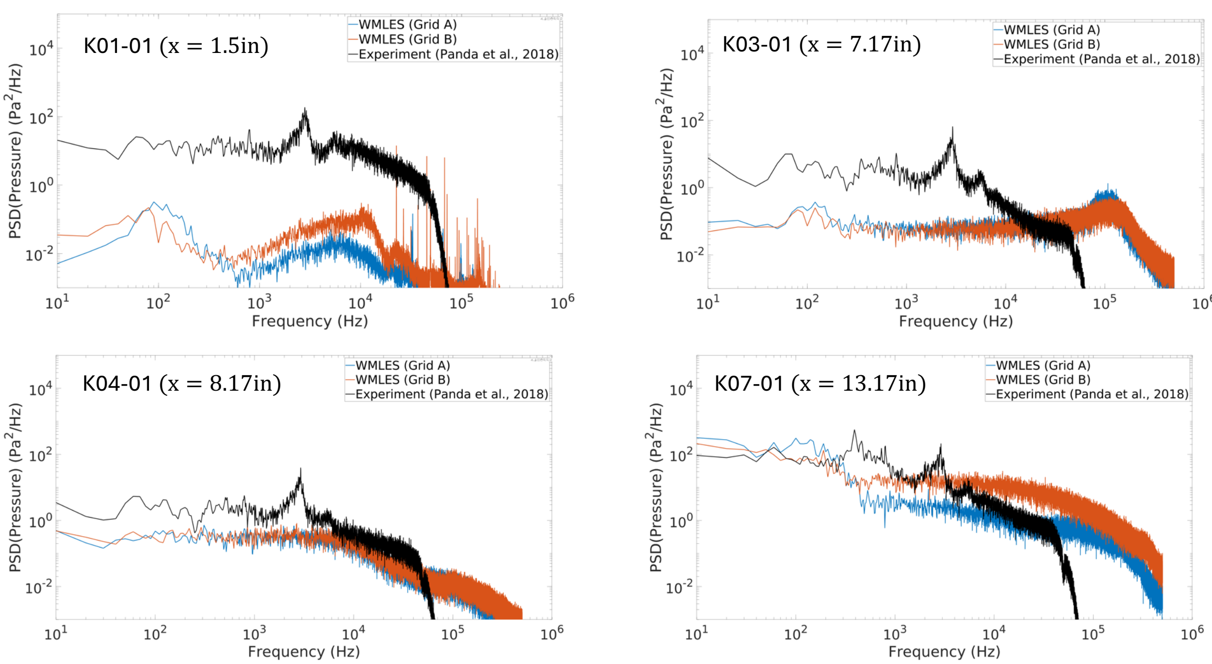

Fig. 13 Pressure auto-spectra on an azimuthal column ($\phi = 0°$) of Kulites located on the nose and flat portions of the fairing.

of maximum pressure variance. This represents a discrete sampling of the two-point space-time correlations for the geometry. Excellent qualitative agreement is observed between the experiment and WMLES with WMLES

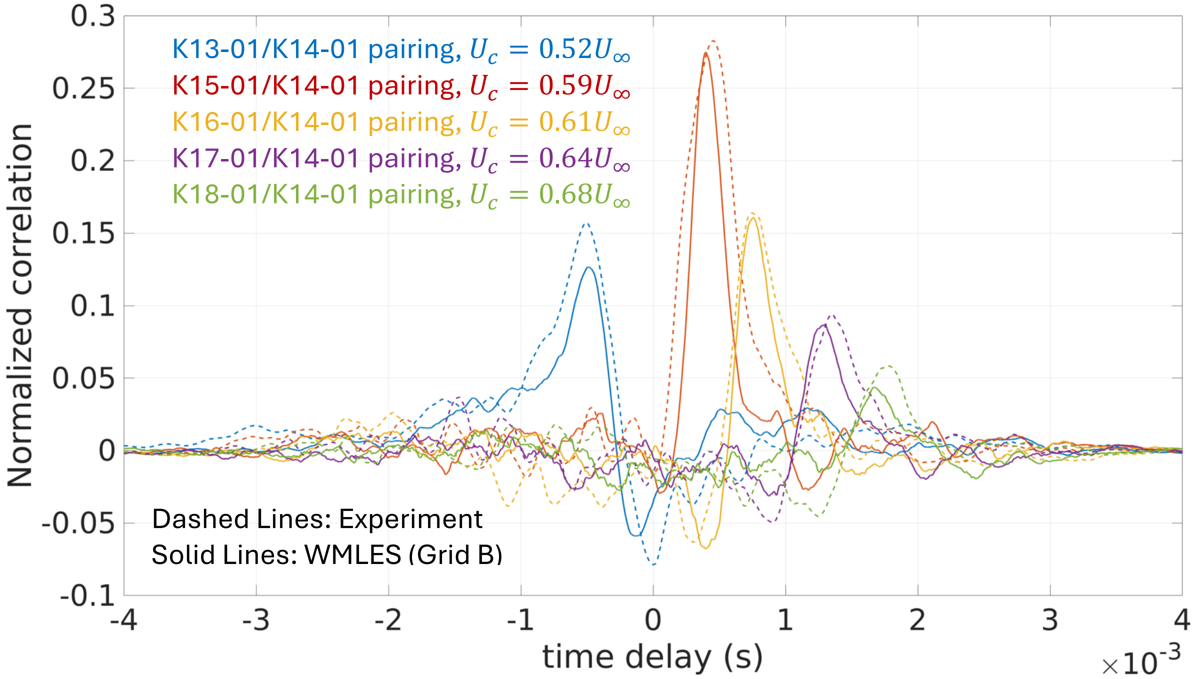

Fig. 14 Temporal cross-correlation of Kulite pairs taken on the second stage at azimuth ($\phi = 0°$) along with the implied convection velocity estimates.

predicting a marginally higher convection velocity of $U_c \approx 0.6U_\infty$ compared to the experiment. Furthermore, WMLES shows a larger decorrelation with increasing distance; Kulite pairing K18-01/K14-01 shows a lower peak correlation at a lower time-delay. This is consistent with under-prediction of pressure variance in low-frequencies indicating that the integral length scale of pressure fluctuations at the azimuthal locations is smaller in the WMLES compared to the experiment. Further investigations are needed to address this discrepancy. Since these two-point correlations play a critical role in design recommendations for the frustrum angles, ratio of payload fairing to second stage diameter, etc. it is particularly promising to see the overall agreement with the experiment.

5) Finally Figure 15 shows two different Kulite pairing that show negative correlation which is consistent with experimental observations indicating highly complex coupling with the separated flow region. Additional Kulite couplings on the payload fairing were not evaluated due to the large discrepancies seen in the auto-spectra. Finer grid simulations would allow for studying upstream propagation as well as coupling between the pressure fluctuations on the payload fairing with those from the separated region on the second stage.

E. Computational Resources

Table 3 shows the computational resources and cost of the two WMLES discussed in the paper. Both simulations were initialized using a precursor grid that was run for a time of 0.25 s to flush out any initialization related transients. Upon interpolation on grids A and B, the simulations were run for a time period of 0.05 s prior to collection of probe data from locations corresponding the Kulites that were used in the recent NASA ARC's experiments. Both simulations used modest hardware resources: Nvidia RTX 4090 are general purpose consumer-grade graphics cards and the simulations were performed using desktop hardware. Both cases were run for approximately 1s of simulated time which took approximately 10 days of wall-time.

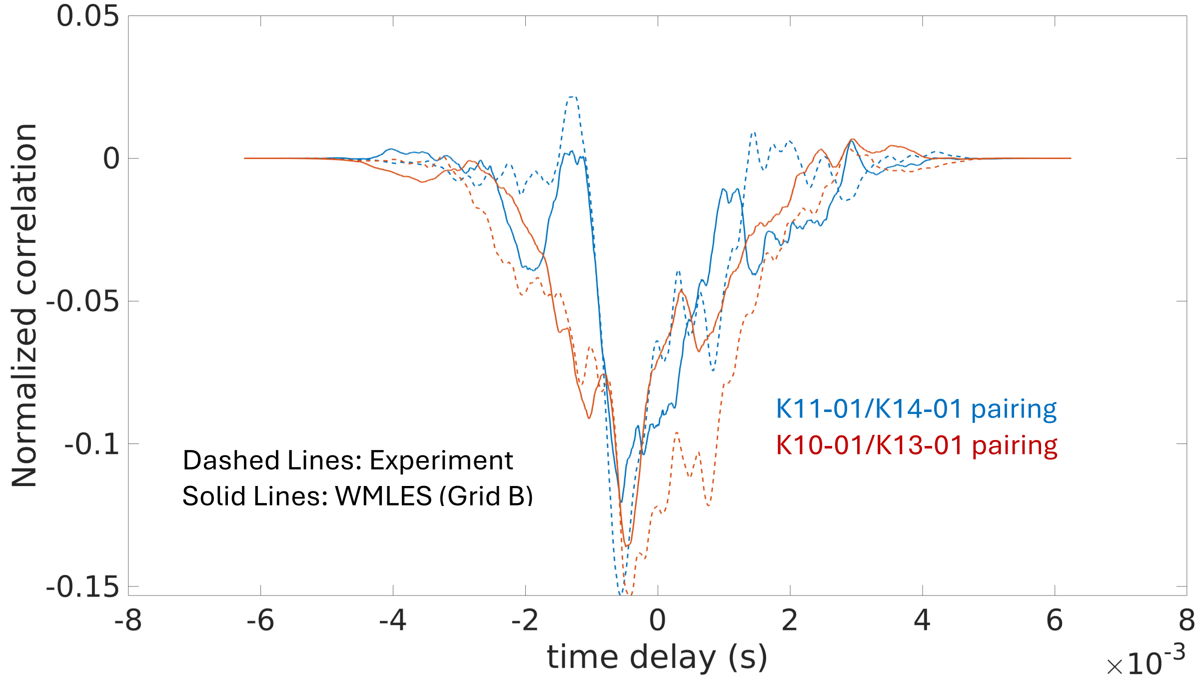

Fig. 15 Temporal cross-correlation of Kulite pairs taken on the neck of the fairing and upstream portion of the second stage indicating complex and potentially upstream propagation.

Table 3 Computational cost of WMLES of the hammerhead problem.

Name	Total compute cells (M)	Numbers of GPUs used	Wall-clock hours per 0.1s of simulation time
Grid A	454	2 x Nvidia RTX 4090	28.5
Grid B	652	7 x Nvidia RTX 4090	23.5

V. Concluding Remarks

Immersed boundary Wall-Modelled Large Eddy Simulations of the generic hammerhead payload fairing were performed using the newly developed Volcano ScaLES solver at the Mach 0.8, $\alpha = 4°$ configuration. Comparisons with recent NASA ARC 11-by-11 ft Transonic wind tunnel experiments show good agreement in peak surface pressure variance as well as second order pressure correlations in the neck region as also in the second stage of the geometry. Some discrepancies exist on the nose and the flat portions of the hammerhead fairing although substantial experimental uncertainties due to the tunnel environment make it difficult to draw major conclusions regarding this flow region. The thin turbulent boundary layers on the nose region of the payload fairing along with potential relaminarization on the flat portion require additional attention in terms of systematic grid convergence studies on substantially finer grids. A secondary purpose of this work was to demonstrate the potential of WMLES to be used as a design tool and this goal was practically achieved. Using very modest desktop-like computational environment, albeit with powerful modern GPUs, the simulations presented herein were quite accurate at predicting two-point space-time correlations in the *loudest* portions of the geometry with strict structural design requirements. Further scientific inquiry into the study of upstream propagation of pressure fluctuations along with the coupling between the transonic shock-waves on the fairing and the separated flow regions on the second stage would require finer resolution simulations with closer collaborations with the experiment team, and are anticipated in the near future.

VI. Acknowledgements

The authors would like to acknowledge Dr. Jay Panda from NASA Ames Research Center for providing time-series Kulite data as well as fruitful discussions regarding the choice of the specific test configuration selected for this study.

References

[1] CH.A. Cole Jr., A. E., and Rainey, A. G., "Buffeting During Atmospheric Ascent," Tech. rep., NASA Ames Research Center and Langley Research Center, 1970. URL `https://ntrs.nasa.gov/api/citations/19710010998/downloads/19710010998.pdf`.

[2] Ericsson, L. E., "Unsteady flow separation can endanger the structural integrity of aerospace launch vehicles," *Journal of Spacecraft and Rockets*, Vol. 38, No. 2, 2001, pp. 168–179.

[3] Coe, C. F., and Nute, J. B., "Steady and Fluctuating Pressures at Transonic Speeds on Hammerhead Launch Vehicles," Tech. rep., NASA Ames Research Center, Moffett Field, CA, 1962. URL `https://ntrs.nasa.gov/api/citations/19650003205/downloads/19650003205.pdf`.

[4] Engineering, N., and Center, S., "Following Design Guidelines to Reduce Atmospheric Buffeting in Launch Vehicles," , 2015. URL `https://llis.nasa.gov/lesson/25602`.

[5] Kiris, C. C., Ghate, A. S., Browne, O. M., Slotnick, J., and Larsson, J., "HLPW-4: Wall-modeled large-eddy simulation and lattice–Boltzmann technology focus group workshop summary," *Journal of Aircraft*, Vol. 60, No. 4, 2023, pp. 1118–1140.

[6] Ghate, A. S., Kenway, G. K., Stich, G.-D., Maldonado, D., and Kiris, C. C., "A wall-modeled LES perspective for the high lift common research model using LAVA," *AIAA Aviation Forum and Exposition 2022*, 2022.

[7] Wong, M. L., Ghate, A. S., Stich, G.-D., Kenway, G. K., and Kiris, C. C., "Numerical study on the aerodynamics of an iced airfoil with scale-resolving simulations," *AIAA SCITECH 2023 Forum*, 2023, p. 0252.

[8] Stich, G.-D., Ghate, A. S., Housman, J. A., and Kiris, C. C., "Wall Modeled Large Eddy Simulations for NASA's jet noise consensus database of single-stream, round, convergent jets." *AIAA SCITECH 2022 Forum*, 2022, p. 0684.

[9] Wong, M. L., K. Kenway, G., Ghate, A. S., Stich, G.-D., and Kiris, C. C., "Predictions of LAGOON Nose Landing Gear Flow and Noise using Wall-Modeled Large Eddy Simulations," *28th AIAA/CEAS Aeroacoustics 2022 Conference*, 2022, p. 2850.

[10] Fukushima, Y., and Kawai, S., "Wall-modeled large-eddy simulation of transonic airfoil buffet at high Reynolds number," *AIAA journal*, Vol. 56, No. 6, 2018, pp. 2372–2388.

[11] Ghate, A. S., Kenway, G. K., Stich, G.-D., Browne, O. M., Housman, J. A., and Kiris, C. C., "Transonic lift and drag predictions using wall-modelled large eddy simulations," *AIAA Scitech 2021 Forum*, 2021, p. 1439.

[12] Goc, K., Agrawal, R., Moin, P., and Bose, S., "Studies of transonic aircraft flows and prediction of initial buffet onset using large-eddy simulations," *AIAA Aviation 2023 Forum*, 2023, p. 4338.

[13] Agrawal, R., Elnahhas, A., and Moin, P., "Wall modeled large-eddy simulations of flow over the Sandia transonic hump," *AIAA Aviation 2023 Forum*, 2023, p. 3972.

[14] Park, G. I., "Wall-modeled large-eddy simulation of a high Reynolds number separating and reattaching flow," *AIAA Journal*, Vol. 55, No. 11, 2017, pp. 3709–3721.

[15] Murman, S. M., and Diosady, L., "Simulation of a hammerhead payload fairing in the transonic regime," *54th AIAA Aerospace Sciences Meeting*, 2016, p. 1548.

[16] Liu, Y., Wang, G., Zhu, H., and Ye, Z., "Numerical analysis of transonic buffet flow around a hammerhead payload fairing," *Aerospace Science and Technology*, Vol. 84, 2019, pp. 604–619.

[17] Lecler, S., Weiss, P.-E., and Deck, S., "Prediction of wall-pressure fluctuations for separating/reattaching flows applied to space launchers using zonal detached eddy simulation-based convolutional neural networks," *Physics of Fluids*, Vol. 35, No. 6, 2023.

[18] Boustani, J., Hall, L., and Steva, T. B., "CFD Predictions of Fluctuating Pressure Environments on NASA's SLS Ascent Unsteady Aerodynamics Wind Tunnel Test," *AIAA SCITECH 2024 Forum*, 2024, p. 2806.

[19] Schuster, D. M., Panda, J., Ross, J. C., Roozeboom, N. H., Burnside, N. J., Ngo, C. L., Kumagai, H., Sellers, M., Powell, J. M., Sekula, M. K., et al., "Investigation of unsteady pressure-sensitive paint (uPSP) and a dynamic loads balance to predict launch vehicle buffet environments," Tech. rep., NASA, 2016.

[20] Panda, J., Garbeff, T., Burnside, N., and Ross, J., "Unsteady pressure fluctuations measured on a hammerhead space vehicle and comparison with Coe and Nute's 1962 data," *International Journal of Aeroacoustics*, Vol. 17, No. 1-2, 2018, pp. 70–87. https://doi.org/10.1177/1475472X17743626, URL https://doi.org/10.1177/1475472X17743626.

[21] Gottlieb, S., and Shu, C.-W., "Total variation diminishing Runge-Kutta schemes," *Mathematics of computation*, Vol. 67, No. 221, 1998, pp. 73–85.

[22] Moin, P., Squires, K., Cabot, W., and Lee, S., "A dynamic subgrid-scale model for compressible turbulence and scalar transport," *Physics of Fluids A: Fluid Dynamics*, Vol. 3, No. 11, 1991, pp. 2746–2757.

[23] Lilly, D., "A proposed modification of the germano sugrid-scale closure method," *Phys Fluids A*, Vol. 4, 1992, pp. 633–635.

[24] Wong, M. L., Ghate, A. S., Kenway, G. K. W., Angel, J. B., and Kiris, C. C., "Immersed Boundary Wall-Modelled Large Eddy Simulations of Subsonic Jet Flows and Acoustics," *AIAA Aviation 2024 Forum*, 2024.

[25] Wong, M. L., Ghate, A. S., Kenway, G. K. W., Angel, J. B., and Kiris, C. C., "Immersed Boundary Wall-Modelled Large Eddy Simulations of a Nose Landing Gear for Aeroacoustics," *AIAA Aviation 2024 Forum*, 2024.

[26] Wong, M. L., Ghate, A. S., Kenway, G. K. W., Angel, J. B., and Kiris, C. C., "Immersed Boundary Wall-Modelled Large Eddy Simulations of Straight Wings with Three-Dimensional Ice Accretion," *AIAA Aviation 2024 Forum*, 2024.

[27] Angel, J. B., Ghate, A. S., Kenway, G. K. W., Wong, M. L., Browne, O. M. F., and Kiris, C. C., "Validation of Immersed Boundary Wall-Modelled Large Eddy Simulations with F-16XL Flight Data," *AIAA Aviation 2024 Forum*, 2024.

[28] Angel, J. B., Ghate, A. S., Kenway, G. K. W., Wong, M. L., and Kiris, C. C., "Immersed Boundary Wall-Modelled Large Eddy Simulations for Automotive Aerodynamics," *AIAA Aviation 2024 Forum*, 2024.

[29] Schmitt, V., and Charpin, F., "Pressure Distributions on the ONERA-M6-Wing at Transonic Mach Numbers," Experimental data base for computer program assessment AGARD Advisory Report AR-138, May 1979.

[30] "NASA Langley Turbulence Modeling Resource website," , 2024. URL https://turbmodels.larc.nasa.gov.

[31] Gray, P. D., Gluzman, I., Thomas, F. O., Corke, T. C., Lakebrink, M. T., and Mejia, K., "Benchmark characterization of separated flow over smooth Gaussian bump," *AIAA Aviation 2022 Forum*, 2022, p. 3342.

[32] Iyer, P. S., and Malik, M. R., "Assessing Reynolds Number Effects for flow over a Gaussian bump using Wall-modeled LES," *AIAA AVIATION 2023 Forum*, 2023, p. 3982.

[33] Panda, J., Roozeboom, N., and Ross, J., "Wavenumber-frequency spectra on a launch vehicle model measured via unsteady pressure-sensitive paint," *AIAA Journal*, Vol. 57, No. 5, 2019, pp. 1801–1817.